

Charge disproportionation and complex magnetism in PbMnO_3 perovskite synthesized under high pressure

Xiang Li^{1,2}, Zhiwei Hu³, Yujin Cho⁴, Xinyu Li², Hao Sun¹, Longzheng Cong¹, Hong-Ji Lin⁵, Sheng-Chieh Liao³, Chien-Te Chen⁵, Anna Efimenko⁶, Christoph J. Sahle⁶, Youwen Long^{7,8}, Changqing Jin⁷, Michael C. Downer⁴, John B. Goodenough², Jianshi Zhou^{2*}

¹ Key Laboratory of Advanced Optoelectronic Quantum Architecture and Measurement, Ministry of Education (MOE), School of Physics, Beijing Institute of Technology, Beijing 100081, China

² Materials Science and Engineering Program, Department of Mechanical Engineering, University of Texas at Austin, Austin, Texas 78712, USA

³ Max Planck Institute for Chemical Physics of Solids, Nöthnitzer Straße 40, Dresden 01107, Germany

⁴ Department of Physics, University of Texas at Austin, Austin, Texas 78712, USA

⁵ National Synchrotron Radiation Research Center, 101 Hsin-Ann Road, Hsinchu 30076, Taiwan

⁶ European Synchrotron Radiation Facility (ESRF), 71 Avenue des Martyrs, Grenoble 38000, France

⁷ Beijing National Laboratory for Condensed Matter Physics, Institute of Physics, Chinese Academy of Sciences, Beijing 100190, China

⁸ Songshan Lake Materials Laboratory, Dongguan, Guangdong 523808, China

ABSTRACT: Due to the possible crossover of Pb and $3d$ transition metal (T_M) redox levels, a charge transfer between Pb and T_M leads to a continuous evolution from $\text{Pb}^{2+}\text{Ti}^{4+}\text{O}_3$ to $\text{Pb}^{4+}\text{Ni}^{2+}\text{O}_3$ in the perovskite family of $\text{Pb}T_M\text{O}_3$ as verified by several reports. However, very little information is known about PbMnO_3 in the $\text{Pb}T_M\text{O}_3$ series. The perovskite PbMnO_3 is the most difficult one for synthesizing although its geometric tolerance factor is close to 1. Here we report a careful study of PbMnO_3 synthesized under 15 GPa by a structural refinement and high-precision X-ray absorption spectroscopy (XAS) as well as a variety of measurements of physical properties. We can rationalize the physical properties of PbMnO_3 based on a local bonding model and the valence states of Pb and Mn from XAS. Moreover, the complete study of PbMnO_3 allows us to construct a more consistent picture of the valence evolution and the charge disproportionation for the entire family of $\text{Pb}T_M\text{O}_3$ perovskites.

1. INTRODUCTION

Investigations of lead-transition metal perovskites $\text{Pb}T_M\text{O}_3$ ($T_M = 3d$ transition metal) have highlighted the important role played by the valence state at the A-site Pb cations in determining the properties of these materials¹⁻³. One striking observation is that the charge distribution between the A-site and B-site cations in $\text{Pb}T_M\text{O}_3$ varies with the d^n manifolds of the transition metal due to the fact that the hybrid Pb-6s and 6p bands are close in energy to the O-2p bands and transition metal d bands⁴. Across the $3d$ transition-metal row from left to right in the periodic table, PbTiO_3 with Ti^{4+} (d^0) and PbVO_3 with V^{5+} (d^0) exhibit the valence states of $\text{Pb}^{2+}T_M^{4+}\text{O}_3$ ^{5,6}, whereas the oxidation state of $\text{Pb}^{4+}\text{Ni}^{2+}\text{O}_3$ with Ni^{2+} (d^8) has been determined⁷. The valence state crossover from Pb^{2+} to Pb^{4+} and from $4+$ to $2+$ for the transition metals between these two end members is not straightforward. The member of the family in which the charge disproportionation of Pb starts to occur is still unknown. The charge distribu-

tion of PbCrO_3 remains controversial. The charge disproportionation $3\text{Cr}^{4+} \rightarrow 2\text{Cr}^{3+} + \text{Cr}^{6+}$ has indicated a Pb^{2+} valence state in $\text{Pb}^{2+}\text{Cr}^{4+}\text{O}_3$ (Cr^{4+} : d^2)⁸. Yu *et al.*, however, claimed a $\text{Pb}^{2+}_{0.5}\text{Pb}^{4+}_{0.5}\text{Cr}^{3+}\text{O}_3$ (Cr^{3+} : d^3) valence state based on structural and X-ray photoelectron spectroscopy (XPS) measurements⁹. However, PbFeO_3 with Fe^{3+} (d^5), has been found to show a charge disproportionation of Pb^{3+} ions into Pb^{2+} and Pb^{4+} in $\text{Pb}^{2+}_{0.5}\text{Pb}^{4+}_{0.5}\text{Fe}^{3+}\text{O}_3$ ¹⁰. The Pb^{4+} concentration appears to increase as the atomic number Z of the transition metal further increases from Fe. The trend continues to $T_M = \text{Co}$ and Ni . In PbCoO_3 ; however, in addition to the charge disproportionation of Pb, Co has been found to have a mixed valence state $\text{Pb}^{2+}_{0.25}\text{Pb}^{4+}_{0.75}\text{Co}^{2+}_{0.5}\text{Co}^{3+}_{0.5}\text{O}_3$ (Co^{3+} : d^5 and Co^{2+} : d^7)⁴. Based on the data available to them, Sakai *et al.*⁴ have proposed a crossover from Pb^{2+} to Pb^{4+} in the family of $\text{Pb}T_M\text{O}_3$ perovskites. Perovskite PbMnO_3 has been synthesized at 15 GPa¹¹. By using an iodometric-titration method, the authors gave a formula $\text{Pb}^{2+}\text{Mn}^{4+}\text{O}_3$ (Mn^{4+} : d^3), which clearly contradicts the formula $\text{Pb}^{2+}_{0.5}\text{Pb}^{4+}_{0.5}\text{Mn}^{3+}\text{O}_3$

predicted by Sakai *et al.*⁴ The primary goal for this work is to determine the charge distribution in PbMnO_3 by X-ray absorption spectroscopy (XAS).

For the perovskite structure, the geometric tolerance factor t defined as $t \equiv (\text{Pb}-\text{O})/\sqrt{2}(\text{T}_\text{M}-\text{O})$, where $(\text{Pb}-\text{O})$ and $(\text{T}_\text{M}-\text{O})$ are equilibrium bond lengths, provides a measurement of the structural stability. A cubic structure is found for $t = 1$; For $t < 1$, the bond length mismatch is accommodated by cooperative octahedral-site rotations that result in bending the $\text{T}_\text{M}-\text{O}-\text{T}_\text{M}$ bond from 180° ; for $t > 1$, the oxide either undergoes a ferroelectric displacement like in PbTiO_3 ¹² and PbVO_3 ⁵ or adopts a polytype structure¹³. An earlier study has shown that an oxygen-stoichiometric hexagonal-perovskite polytype (6H) of PbMnO_3 can be stabilized under 8 GPa at 1073 K owing to a $t > 1$. The valence state of 6H- PbMnO_3 has been confirmed to be $\text{Pb}^{2+}\text{Mn}^{4+}\text{O}_3$ by iodometric titration and the unit-cell composition calculated from its structural model^{11,14}. Generally speaking, the Pb-O bond is more compressible than the $\text{T}_\text{M}-\text{O}$ bond, which makes the factor t decrease under high pressure. The high-pressure phases with a reduced t factor can normally be quenched to ambient condition as has been found in cubic BaRuO_3 ¹⁵. Therefore, a cubic PbMnO_3 is expected if it is made under a sufficiently high pressure. Surprisingly, a tetragonal phase of $\text{PbMnO}_{3.94}$ with a small tetragonal distortion ($c/a = 1.017$) is stabilized under 15 GPa at 1273 K, which is similar to that found in BaRuO_3 ¹⁶. The origin of this structural distortion is still unclear. Furthermore, similar to PbTiO_3 and PbVO_3 , a ferroelectric perovskite PbMnO_3 is expected for a t slightly larger than 1. A recent first-principles density functional theory (DFT) calculation indeed predicted that the polar $P4mm$ phase has a ground-state energy slightly lower than that of the non-polar $P4/mmm$ phase¹⁷. However, a structural analysis based on a synchrotron X-ray diffraction pattern suggests that the tetragonal phase of PbMnO_3 adopts a non-polar structure with the space group of $P4/mmm$ ¹¹. To date, the available data on PbMnO_3 are insufficient to distinguish whether it adopts the polar structure $P4mm$ seen in PbTiO_3 and PbVO_3 or the non-polar structure $P4/mmm$. It is useful to compare PbMnO_3 with other perovskite oxides with Mn^{4+} like SrMnO_3 ¹⁸. Although the size of the Pb^{2+} ion (1.49 Å) is comparable to that of the Sr^{2+} ion (1.44 Å), the perovskite PbMnO_3 has been reported to show an antiferromagnetic (AFM) order with a Néel temperature $T_\text{N} = 20$ K¹¹, which is much lower than $T_\text{N} = 233$ K of SrMnO_3 ¹⁸. Oka *et al.* have argued that a double-exchange ferromagnetic (FM) interaction resulting from e_g electrons hopping between Mn^{3+} and Mn^{4+} neighbors weakens the AFM superexchange interactions through the $t_{2g}-\text{O}-t_{2g}$ ¹¹ so as to lower T_N . Alternatively, a more covalent bonding of the π -bonding Pb-O bond than that of the Sr-O bond clearly plays an important role in suppressing the magnetic transition temperature as seen in $\text{Pb}_{1-x}\text{Sr}_x\text{RuO}_3$ ¹⁹. In order to understand these unusual structural and physical properties in the perovskite PbMnO_3 , we have determined the

valance states of Pb and Mn by using XAS at the Pb- L_3 and Mn- $L_{2,3}$ edges, respectively, and measured transport and magnetic properties.

2. EXPERIMENTAL SECTION

A polycrystalline sample of tetragonal PbMnO_3 was synthesized under 15 GPa and 1473 K in a Walker-type multianvil module (Rockland Research Co.). The mixed powder of PbO_2 , MnO_2 and KClO_4 (Alfa, 99.9 %+) with a molar ratio of 1:1:1 as starting materials was pressed into a small pellet and sealed in a platinum crucible. The crucible was inserted into a BN sleeve and then placed at the center of a Mo heater with two LaCrO_3 plugs at the ends. A cylindrical LaCrO_3 sleeve was used to ensure a better thermal isolation and a Cr-doped MgO octahedron with 12 mm edge length was used as a pressure medium. A single-phase sample was obtained only if the crucible was sealed well and the sintering temperature was above 1473 K.

High-resolution synchrotron X-ray powder diffraction (SXRPD) data at room temperature were collected at beamline 11-BM located at the Advanced Photon Source (APS), Argonne National Laboratory with an average λ wavelength of 0.45789 Å. Rietveld refinement of the SXRPD pattern was done with the software Fullprof²⁰. Second harmonic generation (SHG) microscopy was measured with a Ti:Sapphire laser operating at 780 nm wavelength (76 MHz repetition rate, 150 fs pulse width). The p -polarized laser was incident on the sample at an angle of 45° and the signal was detected by a photomultiplier tube (PMT). Soft XAS spectra at the Mn- $L_{2,3}$ edges were measured at the 11 A beamline of NSRRC Taiwan by using a total electron yield method; the high-resolution partial fluorescence yield (PFY) Pb- L_3 XAS spectra with an overall resolution of ~ 1.0 eV was measured at the ID 20 beamline of the ESRF, France²¹. The emission energy of the spectrometer was tuned to the peak of the Pb- L_{α_1} emission line and the incident photon energy was scanned through the Pb- L_3 edge. The Pb- L_3 spectra of PbMnO_3 and the Pb^{4+} reference in PbNiO_3 were normalized at 95 eV above the absorption edge. Thermogravimetric analysis (TGA) was conducted on a Setaram TG-DTA device at a heating rate of 5 K/min up to 1200 K in a mixture of hydrogen (10%) and argon (90%) gases. Resistivity and specific heat were measured with a Physical Property Measurement System (PPMS) from Quantum Design. Thermoelectric power was measured with a homemade apparatus. Magnetization was measured with a Vibrating Sample Magnetometer (VSM) on PPMS.

DFT calculations were performed with the projector augmented wave method^{22,23} as implemented in the Vienna Ab Initio simulation package^{24,25}. Spin-polarized calculations were conducted based on a supercell containing 40 atoms. A PBEsol+U functional was applied to the d^n manifold of Mn with $U = 6.9$ eV and $J_\text{H} = 1$ eV. A $5 \times 5 \times 5$ k -points mesh, a plane-wave cutoff of 600 eV, and a force convergence tolerance of 2.5 meV/Å were employed in

the structural relaxation. The density of states and band structure were calculated by using the code HSE06²⁶.

3. RESULTS

3.1 Structural characterizations

Figure 1 shows the Rietveld analysis result of the SXRPD pattern at room temperature. We find the major phase of PbMnO_3 (Vol. ~96%) has a tetragonal structure with a space group $P4/mmm$ (No. 123) that is consistent with previous work¹¹. Refinements with the lattice parameters of $a = 3.8975(1)$ Å and $c = 3.8654(1)$ Å give a good profile fitting of diffraction peaks, as illustrated in the inset of left panel in Figure 1, which indicates a small tetragonal distortion ($c/a = 0.992$). A small amount of impurities (Vol. ~4%) ~~containing including~~ KCl and an unknown phase is present in the sample. The high-resolution SXRPD enables us to determine the atomic displacement parameters (ADPs) of heavy atoms and structural disorder. Table 1 summarizes the refined lattice parameters, atomic positions, ADPs (B_{iso}) and occupancy factors (Occ). The large $B_{\text{iso}}(\text{Pb})$ of $1.51(1)$ Å² at Pb site and the $B_{\text{iso}}(\text{Mn})$ of $0.98(1)$ Å² at Mn site reveal large positional disorders in PbMnO_3 . It should be noted that similar reliability R values were obtained by fitting the SXRPD profile with either non-polar $P4/mmm$ or polar $P4mm$ symmetry. Since it is difficult to determine precisely the oxygen positions by X-ray if it adopts the polar structure, we are not able to distinguish the polar versus nonpolar structural models used to refine the SXRPD pattern. Alternatively, the highly sensitive optical SHG has a noteworthy advantage in probing a polar structure.



Figure 1. SXRPD pattern of tetragonal perovskite PbMnO_3 at room temperature with the space group $P4/mmm$ (No. 123). The inset of left panel shows the profile at 2θ angles between 15° and 17° . The inset of right panel shows the crystal structure of PbMnO_3 .

Table 1. Structural refinement of PbMnO_3 with the space group $P4/mmm$ (No. 123)^a at room temperature.

Atom	x	y	z	$B_{\text{iso}}/\text{Å}^2$	Occ
O1 (1c)	0.5	0.5	0	0.80	1.00
O2 (2e)	0.5	0.0	0.5	0.80	2.00
Pb (1a)	0	0	0	1.51(1)	1.00
Mn (1d)	0.5	0.5	0.5	0.98(1)	1.00

^a The lattice parameters: $a = 3.8975(1)$ Å, $c = 3.8654(1)$ Å and $V = 58.717(1)$ Å³; $R_p = 8.64$, $R_{\text{exp}} = 8.43$ and $\chi^2 = 1.90$.

Figure 2 displays a side-by-side comparison of the SHG mapping on the polished sample surface between PbMnO_3 and a polar oxide $\text{CaMnTi}_2\text{O}_6$. The $\text{CaMnTi}_2\text{O}_6$ is ferroelectric²⁷, showing a strong and pronounced temperature-dependent SHG signal. In contrast, the SHG response from PbMnO_3 is nearly temperature-independent and much weaker by at least two orders of magnitude than that from $\text{CaMnTi}_2\text{O}_6$, which can be attributed to a symmetry-breaking on the sample surface. These observations provide convincing evidence that PbMnO_3 adopts the non-polar $P4/mmm$ symmetry rather than the predicted polar $P4mm$ structure at least above room temperature. Based on the non-polar structural model, the Pb atoms are not allowed to displace from the 1a position (0, 0, 0). Therefore, the tetragonal distortion ($c/a = 0.992$) does not have the same origin as that in PbTiO_3 and PbVO_3 and needs to be further scrutinized together with results of other physical properties.

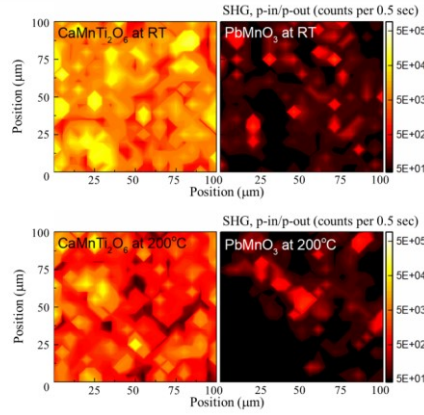


Figure 2. SHG micrographs on PbMnO_3 and $\text{CaMnTi}_2\text{O}_6$: Top panels were measured at room temperature, and the bottom panels were measured at 200°C . The average SHG of PbMnO_3 was extremely weak and nearly temperature independent.

3.2 Charge distribution from XAS

We now turn to determination of the valence states of the Mn and Pb ions in PbMnO_3 by XAS spectra. The soft XAS spectra at the $3d$ transition metal $L_{2,3}$ edges are highly sensitive to the valence state: an increase of the valence state causes a shift of the XAS- $L_{2,3}$ spectrum towards higher energies^{28, 29}. Figure 3a shows the Mn- $L_{2,3}$ XAS spectra of PbMnO_3 together with those of MnO , LaMnO_3 and $\text{Sr}_3\text{Mn}_2\text{O}_7$ for comparison. It has been shown that the valence states of Mn ions in the reference compounds of MnO , LaMnO_3 and $\text{Sr}_3\text{Mn}_2\text{O}_7$ are +2, +3 and +4, respectively; the peak positions of PbMnO_3 at the Mn- $L_{2,3}$ edges are located between those of Mn^{3+} and Mn^{4+} , but closer to Mn^{4+} . The average valence state of Mn ions in PbMnO_3 can be estimated to be +3.75 according to the relative energy shift of the absorption edge.

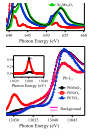


Figure 3. (a) Mn- $L_{2,3}$ XAS of PbMnO_3 compared to that of MnO (Mn^{2+}), LaMnO_3 (Mn^{3+}), and $\text{Sr}_3\text{Mn}_2\text{O}_7$ (Mn^{4+}), respectively; (b) PFY Pb- L_3 XAS of PbMnO_3 together with those of PbNiO_3 (Pb^{4+}) and PbTiO_3 (Pb^{2+}). The inset: the spectral integral area of I_{6s} after subtracting the background.

Figure 3b presents the Pb- L_3 XAS spectrum of PbMnO_3 together with those of PbTiO_3 and PbNiO_3 used as the reference of Pb^{2+} and Pb^{4+} , respectively. Unlike the XAS spectra of the transition metal at L and K edges, where the energy positions of the strong white line and absorption edge are very

sensitive to the number of localized d valence electrons, at the Pb- L edge there is no clear white line and the energy position is strongly affected by the crystal structure, so it is less sensitive to the Pb valence state. Fortunately, the Pb- L_3 XAS spectra taken from the high-resolution PFY mode provide an opportunity to identify the valence state of Pb. As shown in Figure 3b, one finds a sharp lower energy shoulder I_{6s} at 13,030 eV in the PFY spectrum that cannot be observed in normal transmission spectra³. This lower energy pre-edge peak can be assigned to the dipole allowed transition from the $2p^{3/2}$ core level to the unoccupied $6s$ states, while the main peak at 13,040 eV can be assigned to the transitions from the $2p^{3/2}$ core level to the empty Pb- $6d$ states^{3, 30}. The pre-edge peak I_{6s} can be observed for the Pb^{4+} ion with two $6s$ holes, but it is absent for Pb^{2+} ion with a fully occupied $6s$ state. Thus, the spectral intensity of the pre-edge peak I_{6s} can be used to determine the valence change of Pb. To calculate the spectral intensity, the broad background between 13,020 eV and 13,040 eV has been described by an analytic function related to electron states and edge jump^{3, 31}, which can be simulated with a superposition of an arctan-like function and Gaussian lines, as shown in Figure 3b (pink solid curves). After subtracting the background, the spectral integral area of I_{6s} is presented in the inset of Figure 3b. The intensity ratio of I_{6s} between PbMnO_3 and PbNiO_3 is about 1/8, which indicates the average valence state of the Pb ions in PbMnO_3 is +2.25. Moreover, a total weight loss of 10.44% observed by TGA in Figure 4 from the as-made sample to Pb metal and MnO identified by XRD indicates that the as-made sample is nearly oxygen-stoichiometric (3 ± 0.03); this result is consistent with the previous report of iodometric titration¹¹. Since Pb prefers the valence states of Pb^{2+} and Pb^{4+} ³², the charge distribution of the as-made PbMnO_3 can be assigned as $\text{Pb}^{2+}_{0.875}\text{Pb}^{4+}_{0.125}\text{Mn}^{3+}_{0.25}\text{Mn}^{4+}_{0.75}\text{O}_3$ based on the valence state of Pb and Mn ions.

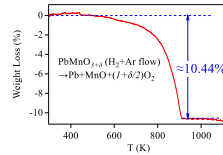


Figure 4. Thermogravimetric data for decomposition of PbMnO_3 on heating from room temperature to 1200 K in a gas flow of hydrogen (10%) and argon (90%).

3.3 Transport properties

The temperature dependence of resistivity $\rho(T)$ under different magnetic fields and zero-field thermoelectric power $S(T)$ of PbMnO_3 are shown in Figs. 5(a, b), respectively. Reliable data of $\rho(T)$ can be only obtained at $T >$

150 K because the extremely high resistance of the sample is comparable to that of the input resistance of the voltmeter used in the measurements at low temperatures; $S(T)$ also becomes noisy for $T < 150$ K. The zero-field resistivity increases dramatically with decreasing temperature, thereby indicating an insulating behavior for the temperature range we examined; no obvious magnetoresistance effect has been observed in an applied field up to 9 T. The inset of Figure 5a presents the plot of zero-field $\ln \rho$ versus inverse temperature T^{-1} , which can be well fitted to the activation transport formula of $\rho \propto \exp(E_p/k_B T)$, where k_B is the Boltzmann's constant and the thermal activation energy E_p is 0.19 eV. This observation is opposite to the result of recent theoretical calculation¹⁷ and to the calculated result presented in this work that gives a metallic PbMnO_3 . On the other hand, Figure 5b shows that the magnitude of the thermoelectric power S at room temperature is smaller than that found in most insulators. In this perovskite with mixed valence $\text{Mn}^{3/4+}$, carriers are progressively trapped as the sample is cooled down from room temperature as indicated by an enlarged magnitude of $S(T)$ at low temperatures. The negative $S(T)$ is an indicator of an n-type semiconductor.

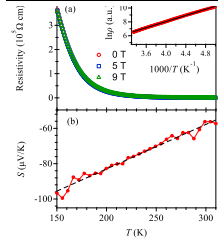


Figure 5. Temperature dependence of (a) resistivity $\rho(T)$ and (b) thermoelectric power $S(T)$ of PbMnO_3 .

3.4 Magnetic properties and specific heat

Figure 6a shows the magnetization as a function of temperature measured with fields of 0.1 T and 9 T in the warming run after zero-field cooling (ZFC) and field cooling (FC). The data with $H = 0.1$ T are qualitatively similar to those obtained by Oka *et al.*, *i.e.* the ZFC and FC curves diverge around 20 K¹⁴. Whereas $\chi(T)$ shows a FM transition at $T_c \sim 20$ K (more obvious in the inset), a clear split-

ting between the ZFC and FC curves is indicative of an AFM spin structure. Additionally, the inverse magnetic susceptibility $\chi^{-1}(T)$ is not linear at $T > T_c$. The part of $\chi^{-1}(T)$ at 0.1 T for $T > 150$ K can be fit to the Curie-Weiss (CW) law with a Weiss constant $\theta_{CW} = -266$ K and an effective moment $\mu_{\text{eff}} = 9.4 \mu_B$. The linear part of $\chi^{-1}(T)$ at 9 T extends to ~ 70 K and fitting to the CW law gives a $\mu_{\text{eff}} = 4.3 \mu_B$ with $\theta_{CW} = 5.4$ K. The sharply different fitting results suggest a possible field-induced transition from an AFM phase to a FM phase. We will return to this point in the discussion section. The obtained μ_{eff} from the $\chi^{-1}(T)$ at 9 T is close to the spin-only value of $4.2 \mu_B$ based on the formula of $\text{Pb}^{2+}_{0.875}\text{Pb}^{4+}_{0.125}\text{Mn}^{3+}_{0.25}\text{Mn}^{4+}_{0.75}\text{O}_3$.

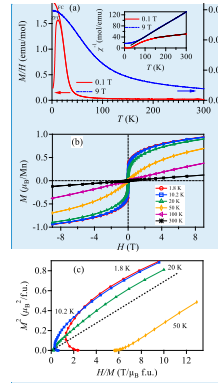


Figure 6. (a) Temperature dependence of magnetization under 0.1 T and 9 T from 1.8 K to 300 K; (b) field dependence of magnetization over the range $-9 \text{ T} \leq H \leq 9 \text{ T}$ and (c) Arrott plot of PbMnO_3 at different temperatures.

Figure 6b displays the field dependence of magnetization at different temperatures. At $T = 1.8$ K, the saturation

Commented [JZ1]: The fitting lines in inset look too thick; they cover the data points

magnetization M_{sat} at 9 T approaches $\sim 0.94 \mu_B/\text{Mn}$. Moreover, non-linear $M(H)$ curves can be found for temperatures up to 50 K, revealing a spin ordering emerges below this temperature. Nearly parallel lines at high fields in the Arrott plot M^2 vs H/M in Figure 6c indicate that PbMnO_3 is a ferromagnet described by the mean field theory for itinerant electron ferromagnetism. An isotherm passing through the origin can be derived from the Arrott plot at a temperature around 20 K which is the critical temperature of FM spin ordering.

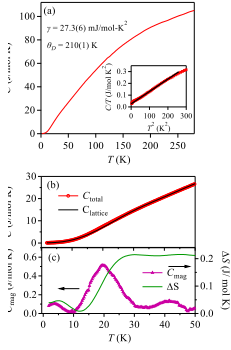


Figure 7. Temperature dependence of (a) specific heat $C(T)$ at zero field from 1.8 K to 300 K; (b) lattice contribution $C_{\text{lattice}}(T)$ obtained by fitting the Debye-Einstein model to $C(T)$; and (c) magnetic specific heat $C_{\text{mag}}(T)$ and magnetic entropy change ΔS at low temperatures of PbMnO_3 .

Specific heat data reveal useful information about magnetic ordering. Figure 7a shows the specific heat $C(T)$ of PbMnO_3 measured in the temperature range from 1.8 K to 300 K. At low temperatures, the specific heat $C(T)$ can be well-described by the formula $C/T = \gamma + \beta T^2$, as shown in the inset of Figure 7a, yielding coefficients of electron contribution $\gamma = 27.3(6)$ mJ/mol-K² and lattice contribution $\beta = 1.04(1)$ mJ/mol-K⁴. A relatively high γ can be re-

lated to free electrons at the Fermi energy. Then, the activated behavior in the $\rho(T)$ of Figure 5a can be attributed to grain-boundary scattering. The Debye temperature θ_D can be derived as 210(5) K. In contrast to the magnetic ordering from the magnetization measurement, a brief overview of the $C(T)$ does not show an obvious signature of a magnetic ordering. After subtracting C_{lattice} , which is obtained by fitting the $C(T)$ in the temperature range 1.8–300 K to the Debye-Einstein model (See Figure 7b up to 50 K), we are able to extract the magnetic contribution $C_{\text{mag}} = C_{\text{total}} - C_{\text{lattice}}$. As can be seen in Figure 7c, C_{mag} has a broad hump in the temperature range between 10 K and 30 K instead of a typical λ -shape profile. Nevertheless, it corresponds well to the anomaly of magnetic susceptibility. The entropy on crossing the transition in Figure 7c is helpful for estimating the degree of spin ordering on crossing the transition. The obtained entropy change $\Delta S \approx 0.2$ J/mol-K is much smaller than the expected value 11.5 J/mol-K for a localized $S = 3/2$ system of Mn^{4+} (t_2^3), which indicates a small number of spins are involved in the transition in zero field.

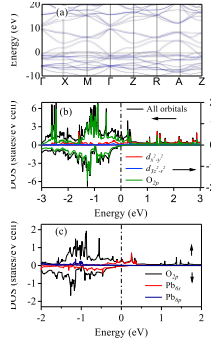


Figure 8. (a) Band structure and (b, c) DOS projected on the Pb, Mn, and O atomic orbitals in the tetragonal perovskite phase of PbMnO_3 ; the arrows \uparrow and \downarrow indicate spin-up and spin-down, respectively.

3.5 The calculated electronic structure

The band structure and the electron density of states (DOS) are shown in Figures. 8(a, b and c), respectively. Several dispersion curves cross the Fermi energy; most of the curves form narrow bands. The major contributions of DOS at E_F come from the O-2p band and Pb-6s band. The prediction of a metallic PbMnO_3 is consistent with a finite γ from the specific heat measurement. A clear exchange splitting is consistent with the magnetic transition. The calculated result of the ground-state energy with different types of magnetic ordering is given in Table 2. A FM phase has the lowest energy; this conclusion also is consistent with the analysis of $\chi(T)$ at high magnetic fields. By relaxing the crystal structure, the most stable crystal structure from the calculation is not the tetragonal phase, but a simple cubic perovskite structure. A much enhanced $\gamma = 27.3 \text{ mJ/mol-K}^2$ relative to the calculated $\gamma_0 = 3.5 \text{ mJ/mol-K}^2$ suggests that electrons in PbMnO_3 are strongly correlated. Despite the great success of structure and property prediction by a first-principles calculation for a broad range of materials, the Augmented Plane Wave (APW) appears to be too far from the real electron distribution for the Pb lone-pair electrons, especially the hybridization with the narrow bands of Mn-3d and O-2p, which may be the origin of the tetragonal distortion found in PbMnO_3 . Nevertheless, our calculation successfully predicts a non-polar PbMnO_3 . By using an electron localization function (ELF) ³³, we have analyzed the bonding character of PbMnO_3 and compared with that of PbVO_3 in Figure 9. Our calculated result for PbVO_3 is identical to that in the literature; the lone-pair 6s² electrons form a hat-like cloud on one side of the Pb²⁺ ions along the c axis. The more covalent bonding between the lone-pair electrons and O-2p pulls the apical oxygen from the middle between VO_2 planes, which appears to be the driving force for the formation of the polar structure. In contrast, the localized 6s electrons are distributed uniformly around Pb in PbMnO_3 .

Table 2. The system energy of PbMnO_3 with different types of magnetic ordering by the DFT calculation

	Lattice constant (Å)	Octahedral volume (Å ³)	Mn-O _{eq} distance (Å)	Energy (eV)
A-type AFM	3.8762	9.4737	1.9226	0.0607
C-type AFM	3.7983	9.4543	1.9214	0.0632
G-type AFM	3.8271	9.3443	1.9137	0.1814
FM	3.8518	9.5266	1.9260	0.0000

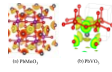


Figure 9. Valence electrons ELF isosurface around (a) Pb in PbMnO_3 ; (b) Pb and O in PbVO_3 .

4. DISCUSSION

4.1 Crystal structure

The $P4/mmm$ structure resolved from the refinement of XRD pattern is unusual for a perovskite oxide with t slightly larger than 1, which normally leads to hexagonal polytypes or a polar structure for oxides made under ambient pressure ¹³. The t factor in ABO_3 oxides reduces under high pressure, so that a $t = 1$ for the cubic phase can be reached under high pressure. Therefore, the high-pressure and high-temperature phase quenched to ambient condition should have the B-O bond under tension, which normally gives rise to a cubic phase. The $P4/mmm$ structure gives no tilting of the octahedra, but it allows an elongated octahedron along the c axis. The averaged Mn-O bond length 1.944 Å is significantly larger than 1.903 Å extracted from the cubic SrMnO_3 with Mn⁴⁺ ¹⁸. In comparison, the Jahn-Teller (JT) active Mn³⁺ in LaMnO_3 has an averaged Mn-O bond length 2.020 Å ³⁴. In the ionic model, we can use the bond valance sum (BVS) to calculate the actual valance of cations ³⁵. Based on the bond lengths from the structural study, we obtained the BVS = 3.6, which is close to the XAS result.

In order to understand better the structure of PbMnO_3 and the evolution of chemical and physical properties in the PbT_MO_3 perovskites, it will be useful to start the discussion from the tolerance factor t . Table 3 lists the t values and other structural parameters of the PbT_MO_3 series. On the side $t > 1$, PbTiO_3 and PbVO_3 favor the tetragonal structure of $P4mm$ and are ferroelectric. On the side $t < 1$, both PbFeO_3 and PbCoO_3 show cooperative octahedral-site rotations in their structures. Accordingly, the reduction of t values agrees well with the increasing ratio of the smaller Pb⁴⁺ ions. It is important to know that the tetragonal PbMnO_3 with $t = 1.01$ is located at the boundary between the polar structure with displacive Pb ions ($t > 1$) and the distorted structure with a cooperative rotation of the MO_6 octahedra ($t < 1$). The consideration based on t

factor alone fails to predict the tetragonal phase found in the experiment. The driving forces for the structural dis-

Table 3. The structural parameters and physical properties of $\text{PbT}_\text{M}\text{O}_3$ perovskites.

Compound	PbTiO_3^{37}	PbVO_3^{38}	PbCrO_3^{39}	PbMnO_3	PbFeO_3^{40}	PbCoO_3^4	PbNiO_3^7
Space group	$P4\text{mm}$	$P4\text{mm}$	$\text{Pm-}3\text{m}$	$P4/\text{mmm}$	Unknown	$\text{Pn-}3$	Pnma
t	1.02	1.04	1.02	1.01	0.93	0.91	0.83
GII	0.139	0.249	0.156	0.560	0.279	0.424	0.061
Valence distribution	$\text{Pb}^{2+}\text{Ti}^{4+}\text{O}_3$	$\text{Pb}^{2+}\text{V}^{5+}\text{O}_3$	$\text{Pb}^{2+}\text{Cr}^{4+}\text{O}_3$	$\text{Pb}^{2+}_{0.875}\text{Pb}^{4+}_{0.125}\text{Mn}^{3+}_{0.25}\text{Mn}^{4+}_{0.75}\text{O}_3$	$\text{Pb}^{2+}_{0.5}\text{Pb}^{4+}_{0.5}\text{Fe}^{3+}\text{O}_3$	$\text{Pb}^{2+}_{0.25}\text{Pb}^{4+}_{0.75}\text{Co}^{3+}_{0.5}\text{Co}^{4+}_{0.5}\text{O}_3$	$\text{Pb}^{4+}\text{Ni}^{2+}\text{O}_3$
Applied pressure for synthesis	Ambient pressure	6 GPa	6 GPa	15 GPa	7 GPa	12 GPa	3 GPa
Physical properties	Ferroelectric insulator $T_c = 764$ K	AFM insulator $T_N = 180$ K	AFM insulator $T_N = 245$ K	FM metal $T_c \sim 20$ K	Unknown	AFM insulator $T_N = 8$ K	AFM insulator $T_N = 225$ K

tortion may include the bonding mismatch due to the interaction between the Pb- s_p hybrid and Mn- e_g orbitals. In addition to the t factor, whether a particular crystal structure for a given chemical formula can be stabilized easily depends on the global instability index (GII) which can be calculated for the perovskite structure with the software of SPuDS ³⁶. In comparison with $GII = 0.005$ for a simple perovskite SrTiO_3 , a much larger $GII = 0.560$ is obtained for PbMnO_3 with the tetragonal structure $P4/\text{mmm}$. A compound with a large GII is unstable and can normally be made only through a special synthesis route, such as a high pressure synthesis. GII values calculated for all $\text{PbT}_\text{M}\text{O}_3$ are listed in Table 3, which is generally consistent with the argument that the synthesis of a perovskite with a high GII must be made under higher pressure.

4.2 Evolution of the valance state in $\text{PbT}_\text{M}\text{O}_3$

Our XAS result shows that PbMnO_3 has a $\text{Pb}^{2+}_{0.875}\text{Pb}^{4+}_{0.125}\text{Mn}^{3+}_{0.25}\text{Mn}^{4+}_{0.75}\text{O}_3$ valence state, which clearly deviates from the interpretation in the paper by Sakai *et al.* that the valence distribution of PbMnO_3 is $\text{Pb}^{2+}_{0.5}\text{Pb}^{4+}_{0.5}\text{Mn}^{3+}\text{O}_3$ estimated from the two neighboring perovskite PbCrO_3 and PbFeO_3 ⁴. The updated picture of valence change in $\text{PbT}_\text{M}\text{O}_3$ is illustrated in Figure 10a; T_M^{4+} holds for PbTiO_3 , PbVO_3 and PbCrO_3 , which is followed by a linear decrease of valence on T_M from +4 in PbCrO_3 to +2 in PbNiO_3 except for a clear deviation observed for PbMnO_3 . Corresponding to the decrease of the valence on T_M , the valence on Pb increases linearly. Such a valence evolution can be attributed to the fact that the d -orbital redox potentials move to lower energy relative to the $\text{Pb}^{2+}/\text{Pb}^{4+}$ redox level as the valence electron number N increases in the 3d transition metal (See Figure 10b.).

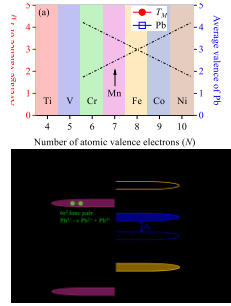


Figure 10. (a) Diagram of the average valence of Pb and transition metals T_M versus the number of atomic valence electrons of the transition metals in the whole $\text{PbT}_\text{M}\text{O}_3$ series; (b) Schematic redox energy diagram representing various types of lead-transition-metal perovskites.

It should be noted that in the cubic structure, adding an electron to the e_g orbital on Mn^{3+} cation would cost an

extra energy Δ due to the crystal field splitting, which makes $\text{Mn}^{3+/4+}$ redox level relatively higher than $\text{Fe}^{3+/4+}$ redox, but still lower than the $\text{Pb}^{2+/3+}$ redox. As a direct consequence, the population of electrons hopping from $\text{Pb}^{2+/3+}$ redox to $\text{Mn}^{3+/4+}$ redox is essentially prohibited, which leads to the anomalous deviation of the valence state for PbMnO_3 . Moreover, a calculation with SPuDS gives a $t = 1.01$ for PbMnO_3 . A perovskite with a $t > 1$ would normally adopt a polar structure, especially with Pb^{2+} with the lone-pair electrons at the A-site, but a small percentage of Mn^{3+} corresponds to a partial occupation of the e_g orbital, which reduces the t factor of PbMnO_3 close to 1 or even less than 1. Separation of the two $6s^2$ lone-pair electrons on Pb is not energetically favored; therefore the $\text{Pb}^{2+/3+}$ redox potential does not exist. The charge transfer between $\text{Pb}^{2+/3+}$ and $\text{Mn}^{3+/4+}$ always ends up with the charge disproportionation $2\text{Pb}^{3+} \rightarrow \text{Pb}^{2+} + \text{Pb}^{4+}$. Whereas our result of XAS still gives a mixture of Pb^{2+} and Pb^{4+} cations in PbMnO_3 , the XRD pattern does not show any sign of superlattice peaks, indicating a random distribution of Pb^{4+} in the matrix of Pb^{2+} .

4.3 Transport properties

Although PbMnO_3 shows an activated temperature dependence of resistivity, it is still possible that electrons are itinerant in the oxide. Grain-boundary scattering may be responsible for the activated $\rho(T)$ found in PbMnO_3 . In the thermoelectric power measurement, however, the grain-boundary effect makes no contribution to the result. The relatively low thermoelectric power at room temperature indicates a higher charge density than that seen in typical insulators. A large γ extracted from the specific heat measurement appears to support this argument. The most important evidence to support an itinerant-electron behavior is from the Arrott plot of magnetization. In addition, a large ratio of μ_{eff} versus M_{sat} and a low T_c places PbMnO_3 at a location near ZrZn_2 in the Rhodes-Wohlfarth plot ⁴⁰.

4.4 Competing magnetic phases

The unusual isotherms at low magnetic fields for $T < T_c$ in the Arrott plot of Figure 6c attract our attention and a further analysis of these isotherms leads to an in-depth understanding of the magnetism of PbMnO_3 . Let us start from the $M(H)$ loop at 1.8 K. The magnetization from the virgin state behaves like an AFM phase in Figure 11a. A field-induced magnetic transition to a FM phase onsets at a critical field H_{cmi} of 2700 Oe and terminates at ~ 3 T. This transition resembles a metamagnetism for itinerant electrons postulated by Wohlfarth and Rhodes ⁴¹. Examples of metamagnetism have been reported in $\text{Lu}(\text{Co}_{0.94}\text{Al}_{0.06})_2$ ⁴² (the inset in Figure 11a) and ZrZn_2 at a critical pressure where the ferromagnetism is suppressed ⁴³. If we leave out the wing from the virgin state (point A) to 9 T, the rest of the $M(H)$ loop in Figure 11b exhibits a typical butterfly-shaped magnetization that has been observed in a molec-

ular ferric wheel (MFW) NaFe_6 ⁴⁴ (the inset in Figure 11b). In the MFW NaFe_6 , the butterfly-shaped magnetization occurs at ~ 12 T and 0.32 K. A strong field induces a spin-state change from $S = 0$ to $S = 1$. The heat associated with the spin-state change is channeled to the thermal bath via phonons which are fewer at such a low temperature; The butterfly-shaped loop is formed owing to a phonon-bottleneck effect ⁴⁴; This effect is further confirmed by a scan-rate dependence of magnetization. The same physics can be applied to the magnetization of PbMnO_3 . The only hypothesis we must make here is that there are two phases in PbMnO_3 , i.e. an AFM dimmer phase and a FM phase where the weak itinerant electron ferromagnetism is operative. The $M(H)$ loop found in Figure 11b is a combination of a loop due to the metamagnetic transition and a loop for a ferromagnet.

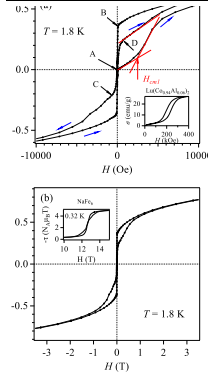


Figure 11. (a) Magnetization of PbMnO_3 at 1.8 K; the definition of critical field H_{cmi} for the metamagnetism transition is shown in the figure. The inset: magnetization of $\text{Lu}(\text{Co}_{0.94}\text{Al}_{0.06})_2$ (the data are after ⁴²); (b) the same as (a) without the wing from the virgin state. The inset: magnetization of the MFW NaFe_6 (the data are after ⁴⁴)

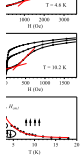


Figure 12. (a, b) Magnetization of PbMnO₃ at 4.6 K and 10.2 K; (c) field-temperature magnetic phase diagram of PbMnO₃; the red line inside is the fitting result to a power law.

The abrupt drop of $M(H)$ at the point B in Figure 11a near the magnetic field reversion distinguishes the butterfly-shaped loop of PbMnO₃ from the typical one in the literature. On top of the spin-state transition from “large” spin in the FM phase to “small” spin in the AFM dimmer phase, the magnetization reversal of the FM phase also occurs at this point. Because of the hysteresis associated with the high spin to low spin transition, a small percentage of the high spin phase persists at $H = 0$ on a part of the demagnetization loop from point B to point C and the moment in the residual high spin phase reverses. Point C and point D are symmetric. Whereas the residual high-spin phase is nearly saturated at D, a further increase of magnetic field is to magnetize the low spin phase. Therefore, the $M(H)$ curve is linear with increasing field from point D with the same slope of $M(H)$ from the virgin state (point A). An identical $M(H)$ loop can be found at all

temperatures below 20 K; the $M(H)$ loops at 4.6 K and 10.2 K are displayed in Figs. 12(a, b). These plots show that H_{cm} lowers progressively as temperature increases. The phase diagram showing the AFM phase and the FM phase is displayed in Figure 12c.

Owing to a charge transfer between Pb and Mn, the perovskite PbMnO₃ exhibits a complex magnetic property. As seen from the Arrott plot in Figure 6c, PbMnO₃ has the same exchange interaction at $T > 20$ K as in other itinerant electron ferromagnets. A competing AFM phase develops right below 20 K and gets strengthened as temperature further decreases. It is highly unusual that a modest magnetic field can convert an AFM phase into a FM phase. The AFM phase appears to be responsible for the splitting between ZFC and FC curves in Figure 5a.

5. CONCLUSION

The perovskite PbMnO₃ offers a unique example that does not adopt either a polar structure or hexagonal polytype although its tolerance factor is slightly larger than 1. In addition, we have demonstrated the importance of a global instability in addition to the t factor in order to synthesize the entire family of PbT_MO₃ perovskites. The crossover of two redox potentials of Pb and T_M as Z of the 3d transition metal T_M increases triggers a charge transfer between Pb and T_M in PbT_MO₃. In addition, a further oxidation of the lone-pair electrons on Pb induces a charge disproportionation $2\text{Pb}^{3+} \rightarrow \text{Pb}^{2+} + \text{Pb}^{4+}$. The new XAS results on PbMnO₃ allow us to fill the gap in the picture of the charge transfer and the charge disproportionation for the entire family of PbT_MO₃ perovskites.

Although an activated resistivity is observed, PbMnO₃ could become the only metallic oxide in the series of PbT_MO₃ as indicated by a large density of states at the Fermi energy extracted from specific-heat measurement and a relatively small magnitude of thermoelectric power. Moreover, itinerant electron ferromagnetism in PbMnO₃ is supported by an observation of nearly linear isothermals in the Arrott plot of magnetization. Although a DFT calculation also predicts a FM metallic phase in PbMnO₃, there is a competing AFM phase below 20 K. The conversion from the AFM phase to a FM phase occurs at a modest magnetic field.

AUTHOR INFORMATION

Corresponding Author

* Jianshi Zhou - Materials Science and Engineering Program, Department of Mechanical Engineering, University of Texas at Austin, Austin, Texas 78712, USA; Email: jszhou@mail.utexas.edu

Author Contributions

J.Z. and X.L. conceived the idea and discussed with other authors. X.L., Z.H., Y.C., X.Y.L., H.S. and L.C. performed the experiments. X.L. and J.Z. wrote the manuscript. All authors analyzed the data and have given the approval to the final version of the manuscript.

ACKNOWLEDGMENT

This work was supported in part by National Natural Science Foundation of China (NSFC) Grant 11904020, 11934017 and Beijing Institute of Technology Research Fund Program for Young Scholars in China and the National Science Foundation grants NSF DMR 1729588, DMR 1905598 in USA. J.B.G. and M.C.D. were supported by Welch Foundation, Houston, Texas, in USA with grant number F-1066 and F-1038. The ESRF is acknowledged for providing synchrotron radiation and C. H. is thanked for technical support during the XAS measurements at ID20. Z.H. acknowledges the support from the Max Planck-POSTECH-Hsinchu Center for Complex Phase Materials. Use of the Advanced Photon Source at Argonne National Laboratory was supported by the U. S. Department of Energy, Office of Science, Office of Basic Energy Sciences, under Contract No. DE-AC02-06CH11357.

REFERENCES

- (1) Goodenough, J. B.; Zhou, J., Varied roles of Pb in transition-metal PbMO_3 perovskites (M= Ti, V, Cr, Mn, Fe, Ni, Ru). *Science and Technology of Advanced Materials* 2015, 16, 036003.
- (2) Azuma, M.; Sakai, Y.; Nishikubo, T.; Mizumaki, M.; Watanuki, T.; Mizokawa, T.; Oka, K.; Hojo, H.; Naka, M., Systematic charge distribution changes in Bi- and Pb-3d transition metal perovskites. *Dalton Transactions* 2018, 47, 1371-1377.
- (3) Chen, K.; Mijiti, Y.; Agrestini, S.; Liao, S. C.; Li, X.; Zhou, J.; Di Cicco, A.; Baudelet, F.; Tjeng, L. H.; Hu, Z., Valence State of Pb in Transition Metal Perovskites PbTMO_3 (TM= Ti, Ni) Determined From X-Ray Absorption Near-Edge Spectroscopy. *Physica Status Solidi (b)* 2018, 180014.
- (4) Sakai, Y.; Yang, J.; Yu, R.; Hojo, H.; Yamada, I.; Miao, P.; Lee, S.; Torii, S.; Kamiyama, T.; Ležaić, M.; Bihlmayer, G.; Mizumaki, M.; Komiyama, J.; Mizokawa, T.; Yamamoto, H.; Nishikubo, T.; Hattori, Y.; Oka, K.; Yin, Y.; Dai, J.; Li, W.; Ueda, S.; Aimi, A.; Mori, D.; Inaguma, Y.; Hu, Z.; Uozumi, T.; Jin, C.; Long, Y.; Azuma, M., A-Site and B-Site Charge Orderings in an s-d Level Controlled Perovskite Oxide PbCoO_3 . *Journal of the American Chemical Society* 2017, 139, 4574-4581.
- (5) Belik, A. A.; Azuma, M.; Saito, T.; Shimakawa, Y.; Takano, M., Crystallographic features and tetragonal phase stability of PbVO_3 , a new member of PbTiO_3 family. *Chemistry of Materials* 2005, 17, 269-273.
- (6) Shpanchenko, R. V.; Chernaya, V. V.; Tsirlin, A. A.; Chizhov, P. S.; Sklovsky, D. E.; Antipov, E. V.; Khlybov, E. P.; Pomjakushin, V.; Balagurov, A. M.; Medvedeva, J. E.; Kaul, E. E.; Geibel, C., Synthesis, structure, and properties of new perovskite PbVO_3 . *Chemistry of Materials* 2004, 16, 3267-3273.
- (7) Inaguma, Y.; Tanaka, K.; Tsuchiya, T.; Mori, D.; Katsumata, T.; Ohba, T.; Hiraki, K.-i.; Takahashi, T.; Saitoh, H., Synthesis, structural transformation, thermal stability, valence state, and magnetic and electronic properties of PbNiO_3 with perovskite- and LiNbO_3 -type structures. *Journal of the American Chemical Society* 2011, 133, 16920-16929.
- (8) Cheng, J.; Kweon, K.; Larregola, S. A.; Ding, Y.; Shirako, Y.; Marshall, L.; Li, Z.-Y.; Li, X.; Dos Santos, A. M.; Suchomel, M.; Matsubayashi, K.; Uwatoko, Y.; Hwang, G. S.; Goodenough, J. B.; Zhou, J.-S., Charge disproportionation and the pressure-induced insulator-metal transition in cubic perovskite PbCrO_3 . *Proceedings of the National Academy of Sciences* 2015, 112, 1670-1674.
- (9) Yu, R.; Hojo, H.; Watanuki, T.; Mizumaki, M.; Mizokawa, T.; Oka, K.; Kim, H.; Machida, A.; Sakaki, K.; Nakamura, Y.; Agui, A.; Mori, D.; Inaguma, Y.; Schlögl, M.; Rushchanskii, K. Z.; Ležaić, M.; Matsuda, M.; Ma, J.; Calder, S.; Isobe, M.; Ikuhara, Y.; Azuma, M., Melting of Pb charge glass and simultaneous Pb-Cr charge transfer in PbCrO_3 as the origin of volume collapse. *Journal of the American Chemical Society* 2015, 137, 12719-12728.
- (10) Tsuchiya, T.; Saito, H.; Yoshida, M.; Katsumata, T.; Ohba, T.; Inaguma, Y.; Tsurui, T.; Shikano, M., High-Pressure Synthesis of a Novel PbFeO_3 . *MRS Online Proceedings Library Archive* 2006, 0988-QQ09-16.
- (11) Oka, K.; Azuma, M.; Hirai, S.; Belik, A. A.; Kojitani, H.; Akaogi, M.; Takano, M.; Shimakawa, Y., Pressure-Induced transformation of 6H hexagonal to 3C perovskite structure in PbMnO_3 . *Inorganic Chemistry* 2009, 48, 2285-2288.
- (12) Glazer, A.; Mabud, S., Powder profile refinement of lead zirconate titanate at several temperatures. II. Pure PbTiO_3 . *Acta Crystallographica Section B* 1978, 34, 1065-1070.
- (13) Goodenough, J. B.; Kafalas, J. A.; Longo, J. M., High-Pressure Synthesis. In *Preparative methods in solid state chemistry*, Hagenmüller, P., Ed. Academic Press, Inc: New York and London, 1972; pp 1-69.
- (14) Bougerol, C.; Gorius, M.; Grey, I., PbMnO_2 . 75—a high-pressure phase having a new type of crystallographic shear structure derived from perovskite. *Journal of Solid State Chemistry* 2002, 169, 131-138.
- (15) Jin, C.-Q.; Zhou, J.-S.; Goodenough, J.; Liu, Q.; Zhao, J.; Yang, L.; Yu, Y.; Yu, R.; Katsura, T.; Shatskiy, A.; Ito, E., High-pressure synthesis of the cubic perovskite BaRuO_3 and evolution of ferromagnetism in ARuO_3 (A= Ca, Sr, Ba) ruthenates. *Proceedings of the National Academy of Sciences* 2008, 105, 7115-7119.
- (16) Cheng, J.-G.; Ishii, T.; Kojitani, H.; Matsubayashi, K.; Matsuo, A.; Li, X.; Shirako, Y.; Zhou, J.-S.; Goodenough, J.; Jin, C., High-pressure synthesis of the BaRuO_3 perovskite: A Pauli paramagnetic metal with a Fermi liquid ground state. *Physical Review B* 2013, 88, 205114.
- (17) Subramanian, S. S.; Natesan, B., Magnetic Ground State and Electronic Structure Calculations of PbMnO_3 using DFT. *Advanced Materials Research* 2014, 895, 420-423.
- (18) Chmaissem, O.; Dabrowski, B.; Kolesnik, S.; Mais, J.; Brown, D.; Kruk, R.; Prior, P.; Pyles, B.; Jorgensen, J., Relationship between structural parameters and the Néel temperature in $\text{Sr}_{1-x}\text{Ca}_x\text{MnO}_3$ ($0 < x < 1$) and $\text{Sr}_{1-y}\text{Ba}_y\text{MnO}_3$ ($y < 0.2$). *Physical Review B* 2001, 64, 134412.
- (19) Cheng, J.-G.; Zhou, J.-S.; Goodenough, J., Evolution of ferromagnetism in orthorhombic perovskites $\text{Sr}_{1-x}\text{Pb}_x\text{RuO}_3$. *Physical Review B* 2010, 81, 134412.
- (20) Rodríguez-Carvajal, J. In *FULLPROF: a program for Rietveld refinement and pattern matching analysis, satellite meeting on powder diffraction of the XV congress of the IUCr*, 1990; Toulouse, France: [sn]: 1990.
- (21) Moretti Sala, M.; Martel, K.; Henriquet, C.; Al Zein, A.; Simonelli, L.; Sahle, C.; Gonzalez, H.; Lagier, M.-C.; Ponchut, C.; Huotari, S., A high-energy-resolution resonant inelastic X-ray scattering spectrometer at ID20 of the European Synchrotron Radiation Facility. *Journal of Synchrotron Radiation* 2018, 25, 580-591.
- (22) Blöchl, P. E., Projector augmented-wave method. *Physical Review B* 1994, 50, 17953.
- (23) Kresse, G.; Joubert, D., From ultrasoft pseudopotentials to the projector augmented-wave method. *Physical Review B* 1999, 59, 1758.
- (24) Kresse, G.; Hafner, J., Ab initio molecular-dynamics simulation of the liquid-metal-amorphous-semiconductor transition in germanium. *Physical Review B* 1994, 49, 14251.

Formatted: Font: (Default) Times New Roman, 9 pt, Not Italic

Formatted: Font: Times New Roman

- (25) Kresse, G.; Furthmüller, J., Efficient iterative schemes for ab initio total-energy calculations using a plane-wave basis set. *Physical Review B* 1996, 54, 11169.
- (26) Heyd, J.; Scuseria, G. E.; Ernzerhof, M., Hybrid functionals based on a screened Coulomb potential. *The Journal of chemical physics* 2003, 118, 8207-8215.
- (27) Aimi, A.; Mori, D.; Hiraki, K.-i.; Takahashi, T.; Shan, Y. J.; Shirako, Y.; Zhou, J.; Inaguma, Y., High-Pressure Synthesis of A-Site Ordered Double Perovskite $\text{CaMnTi}_2\text{O}_6$ and Ferroelectricity Driven by Coupling of A-Site Ordering and the Second-Order Jahn-Teller Effect. *Chemistry of Materials* 2014, 26, 2601-2608.
- (28) Mitra, C.; Hu, Z.; Raychaudhuri, P.; Wirth, S.; Csiszar, S.; Hsieh, H.; Lin, H.-J.; Chen, C.; Tjeng, L., Direct observation of electron doping in $\text{La}_{0.7}\text{Ce}_{0.3}\text{MnO}_3$ using x-ray absorption spectroscopy. *Physical Review B* 2003, 67, 092404.
- (29) Vasiliev, A.; Volkova, O.; Lobanovskii, L.; Troyanchuk, I.; Hu, Z.; Tjeng, L.; Khomskii, D.; Lin, H.-J.; Chen, C.; Tristan, N., Valence states and metamagnetic phase transition in partially B-site-disordered perovskite $\text{EuMn}_{0.5}\text{Co}_{0.5}\text{O}_3$. *Physical Review B* 2008, 77, 104442.
- (30) Liang, G.; Liu, R.; Wang, L., XANES study of the valence of Pb in $(\text{Ti}_{0.5}\text{Pb}_{0.5})\text{Sr}_2\text{Ca}_{1-x}\text{Y}_x\text{Cu}_2\text{O}_{7-8}$. *International Journal of Modern Physics B* 1999, 13, 3693-3696.
- (31) Chen, C.; Sette, F.; Ma, Y.; Hybertsen, M.; Stechel, E.; Foulkes, W.; Schuler, M.; Cheong, S.; Cooper, A.; Rupp Jr, L., Electronic states in $\text{La}_{2-x}\text{Sr}_x\text{CuO}_4 + \delta$ probed by soft-X-ray absorption. *Physical Review Letters* 1991, 66, 104.
- (32) Varma, C., Missing valence states, diamagnetic insulators, and superconductors. *Physical Review Letters* 1988, 61, 2713.
- (33) Savin, A.; Nesper, R.; Wengert, S.; Fässler, T. F., ELF: The electron localization function. *Angewandte Chemie International Edition in English* 1997, 36, 1808-1832.
- (34) Zhou, J.-S.; Goodenough, J., Unusual evolution of the magnetic interactions versus structural distortions in R MnO_3 perovskites. *Physical Review Letters* 2006, 96, 247202.
- (35) Palenik, G. J., Bond valence sums in coordination chemistry using oxidation state independent R-o values. A simple method for calculating the oxidation state of manganese in complexes containing only Mn-O bonds. *Inorganic Chemistry* 1997, 36, 4888-4890.
- (36) Lufaso, M. W.; Woodward, P. M., Prediction of the crystal structures of perovskites using the software program SPuDS. *Acta Crystallographica Section B: Structural Science* 2001, 57, 725-738.
- (37) Shahzad, K.; Khan, M. N.; Shabbir, G.; Bashir, J., Neutron and X-Ray diffraction crystal structure rietveld analysis of PbTiO_3 ceramics. *Ferroelectrics* 2011, 414, 155-161.
- (38) Oka, K.; Yamada, I.; Azuma, M.; Takeshita, S.; Satoh, K. H.; Koda, A.; Kadono, R.; Takano, M.; Shimakawa, Y., Magnetic ground-state of perovskite PbVO_3 with large tetragonal distortion. *Inorganic Chemistry* 2008, 47, 7355-7359.
- (39) Arévalo-López, Á. M.; Dos santos-García, A. J.; Alario-Franco, M. Á., Antiferromagnetism and spin reorientation in " PbCrO_3 ". *Inorganic Chemistry* 2009, 48, 5434-5438.
- (40) Wohlfart, E., Very Weak Itinerant Ferromagnets - Application to ZrZn_2 . *Journal of Applied Physics* 1968, 39, 1061-.
- (41) Wohlfarth, E. P.; Rhodes, P., Collective Electron Metamagnetism. *Philosophical Magazine* 1962, 7, 1817.
- (42) Iijima, M.; Endo, K.; Sakakibara, T., Metamagnetism of itinerant d-electrons in Laves phase compounds $\text{Lu}(\text{Co}_{1-x}\text{Al}_x)_2$. *Journal of Physics: Condensed Matter* 1990, 2, 10069.
- (43) Uhlarz, M.; Pfeleiderer, C.; Hayden, S., Quantum Phase Transitions in the Itinerant Ferromagnet ZrZn_2 . *Physical Review Letters* 2004, 93, 256404.
- (44) Waldmann, O.; Koch, R.; Schromm, S.; Müller, P.; Bernt, I.; Saalfrank, R., Butterfly hysteresis loop at nonzero bias field in antiferromagnetic molecular rings: cooling by adiabatic magnetization. *Physical Review Letters* 2002, 89, 246401.